X-ray Compton Tomography

Axel LANGE [1], Manfred P. HENTSCHEL [1], Andreas KUPSCH [1,*], Gerd-Rüdiger JAENISCH [1], Nikolay KARDJILOV [2], Christian TÖTZKE [2], Henning MARKÖTTER [2], André HILGER [2], Ingo MANKE [2]

[1] BAM Federal Institute for Materials Research and Testing, D-12200 Berlin, Germany
[2] Helmholtz-Zentrum Berlin für Materialien und Energie, D-14109 Berlin, Germany
* Phone: +49 30 8104 3692, Fax: +49 30 8104 1837; e-mail: andreas.kupsch@bam.de

Abstract
The potentials of incoherent X-ray scattering (Compton) tomography are investigated. Imaging materials of very different density or atomic number at once is a perpetual challenge for X-ray tomography or radiography, in general. In a basic laboratory set-up for simultaneous perpendicular Compton scattering and direct beam attenuation tomographic scans are conducted by single channel photon counting. This results in asymmetric distortions of the projection profiles of the scattering CT-data set. In a first approach corrections of Compton scattering data by taking advantage of rotational symmetry yield tomograms without major geometric artefacts. A cylindrical sample composed of PE, PA, PVC, glass and wood demonstrates similar Compton contrast for all the substances, while the conventional absorption tomogram only reveals the two high order materials. Comparison to neutron tomography reveals astonishing similarities except for the glass component (without hydrogen). Therefore, Compton CT bears the potential to replace neutron tomography, which requires much more efforts.

Keywords: X-ray Compton scattering, Computed tomography, Neutron tomography

1. Introduction

The rapidly growing field of applications in non-destructive testing by X-ray radiographic and tomographic techniques comes along with increased requirements for measurement speed and spatial resolution as well as for structural complexity and highly different materials interaction. In recent decades very different approaches have been developed to satisfy the demands. Within the course of events the essential physical interactions with matter has been extended from solely measuring attenuation by absorption towards application of coherent and incoherent scattering [1, 2], refraction [3-9], interferometry [10, 11] and fluorescence for the purpose of imaging.

The various techniques have served as well for creating tomographic projection data sets in order to reconstruct three-dimensional views of material properties such as density, porosity, crystallites [12-14] or element distribution by fluorescent tomography [15, 16], specific surface [17-19], and interface orientation [19, 20].

Referring to Compton imaging previous techniques have preferably applied “triangulation” of the primary and scattered beams [1, 2]. Relatively low attention has been paid to Compton tomography although it provides the potential of contrasting materials of a broad range of atomic numbers simultaneously [21-29].

2. Compton scattering – basics

Considering the limitations of X-ray transmission through materials of considerably different atomic numbers by extremely different attenuation the application of Compton scattering [30] has the advantage of similar contrast, when test samples are composed of high and low atomic weight phases. A comparison of absorption and Compton interaction is demonstrated by the cross-sections in dependence of atomic numbers at 17.5 keV photon energy in Fig. 1, giving the individually extremely different “true” (photoelectric) absorption at the left and the smaller differences of incoherent scattering between elements at the right.

The transmission intensity I of materials of density ρ and chord length d by X-rays of primary intensity I_o is controlled by the mass attenuation coefficient μ according to

$$I = I_o \exp[-\rho\, \mu\, d]. \qquad (1)$$

All the energy dependent interactions of photoelectric effect τ, coherent σ_{coh}, incoherent σ_{inc} and pair production π add up to μ:

$$\mu(E) = \tau(E) + \sigma_{coh}(E) + \sigma_{inc}(E) + \pi(E) \qquad (2)$$

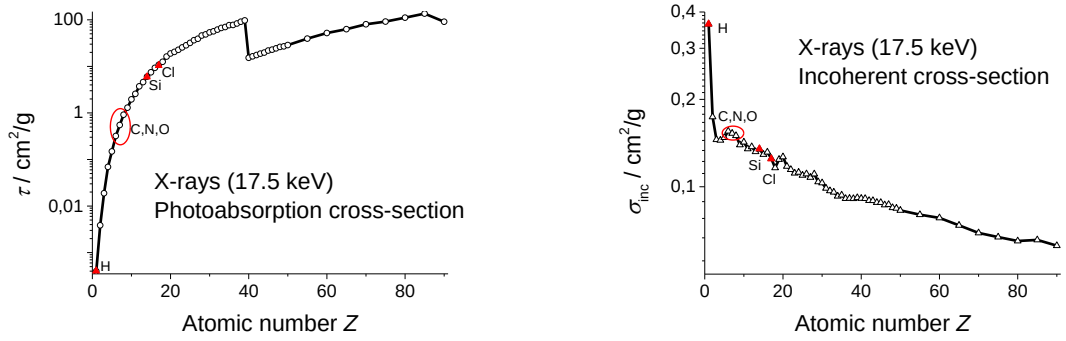

Fig. 1: Absorption and Compton X-ray interaction with matter by cross-sections over atomic numbers at 17.5 keV photon energy; left: extremely different "true" (photoelectric) absorption; right: relatively similar inelastic scattering (data from [31]).

The basic principles of Compton scattering of photons at electrons (incoherent scattering) are demonstrated by Fig.2. The angular dependence of the scattered photon's wavelength or energy shift is given by

$$\lambda' - \lambda = \frac{h}{m_e c}(1 - \cos\theta) \text{ or } E' = \frac{E}{1 + \varepsilon(1 - \cos\theta)}, \qquad (3)$$

with $\varepsilon = E / m_e c^2$, i.e. the multiple (fraction) of an electron's rest energy, given by the electron mass m_e and the speed of light c.

According to (3), the „maximum wavelength shift" occurs at scattering angle $\theta = \pi$. It is limited by the Compton wavelength 2.42 pm and independent of the incident photon energy.

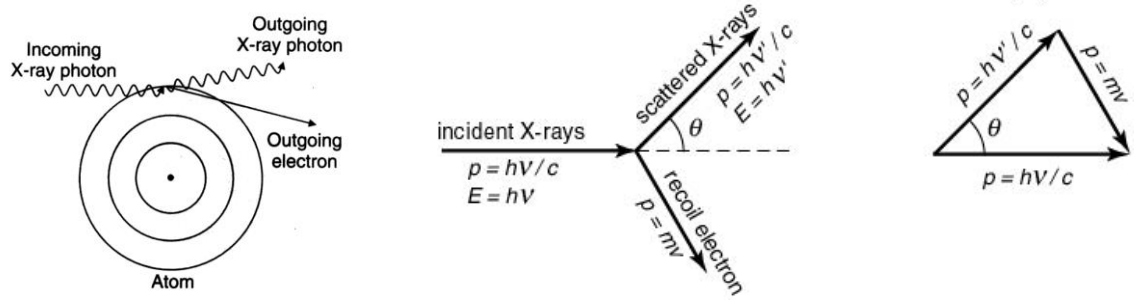

Fig. 2: Basic interactions of photons and electrons in case of incoherent scattering and conservation of energy and momentum [32, 33].

A comparison of the angular distribution of Compton and Rayleigh scattering is given by Fig. 3, which provides the angular scattering distribution by cross sections of 40 keV X-rays at Al. Fig 3 shows at left the incoherent free electron (Klein Nishina, [34]) and Al Compton

scattering considering scattering electron binding effects by correcting the Klein-Nishina cross section by the nonrelativistic Hartree-Fock incoherent scattering functions and at right the coherent free electron (Thomson) and Al scattering cross sections at bound electron by correcting the Thompson cross section by relativistic Hartree-Fock atomic form factor [35, 36]. For detection purposes the essential property of incoherent scattering is given by the rather isotropic scattering outside the narrow coherent forward sector.

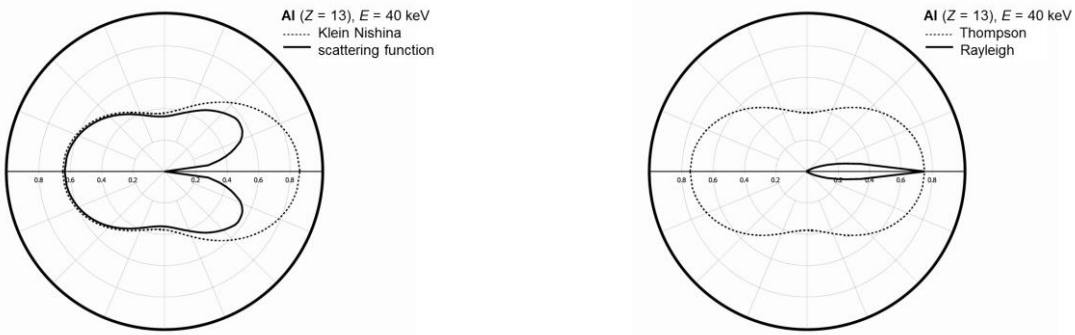

Fig. 3: Comparison of angular distribution of Compton and Rayleigh scattering of Al at 40 keV; left: incoherent free electron (Klein Nishina) and Al Compton scattering cross sections; right: coherent free electron (Thomson) and Al scattering cross sections [35].

3. Twin X-ray interaction tomography

A twin interaction laboratory set-up for (first generation) parallel beam 2D attenuation tomography and Compton scattering tomography is employed for test measurements on low density non-metallic materials of atomic numbers up to 17. The experimental principles are presented by Fig. 4. A 40 µm pencil beam from a Mo X-ray fine structure tube is used for vertical line scans of the sample by 17.5 keV radiation. Without further collimation the attenuation detector measures the primary beam including minor contributions of scattering (both, coherent and incoherent). The scattering detector is arranged perpendicular to the primary beam direction. Without secondary collimation it detects the incoherent scattering at approximately $\theta = 90°$ simultaneously. Both intensities at each projection angle out of a 360° rotation are registered by single photon counting scintillation detectors. The line profiles of both interactions are stored and arranged in separate sinograms for the image reconstruction of the scanned sample layer.

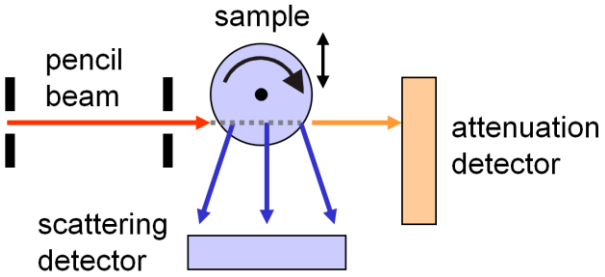

Fig. 4: Schematics of the twin interaction tomography set-up; vertical scans of sample through 40 µm pencil beam; simultaneous registration of attenuated direct beam intensity and 90°. Compton scattered intensity by line scans at each projection angle.

4. Reconstruction strategy

For basic determination of the position dependent attenuation of the Compton scattering signals a model shape sample representing a homogeneous circular PE (polyethylene) cylinder is employed. Unlike the chord length distributions of cylinders in density profiles of absorption measurements the Compton scattering profiles are not symmetric as shown by Fig. 5 and are retained after 180° rotation. When the pencil beam penetrates the sample on the identical path AB inside the material the scattered photons are differently attenuated when leaving the sample at the opposite end after inversion of the direction (Fig. 5, right).

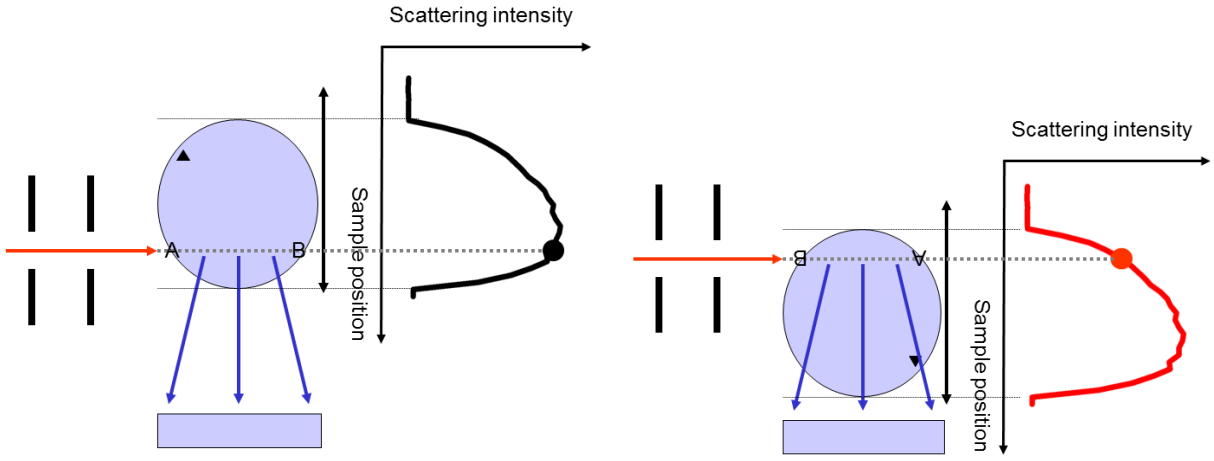

Fig. 5: Sampling profiles (Compton scattered intensity) of a cylindrical specimen rotated by 180°. While the pencil beam penetrates the sample on the identical path AB the scattered photons are differently attenuated when leaving the sample.

For correction of the asymmetric attenuation the corresponding profiles at projection angles φ_i and (φ_i +180°) are averaged, resulting in shorter 180° sinograms of symmetric profiles as conducted in Fig. 6. Due to the absorptive modification of the Compton signals squared averaging is applied. The resulting reconstructions without and with correction are depicted at the bottom of the image.

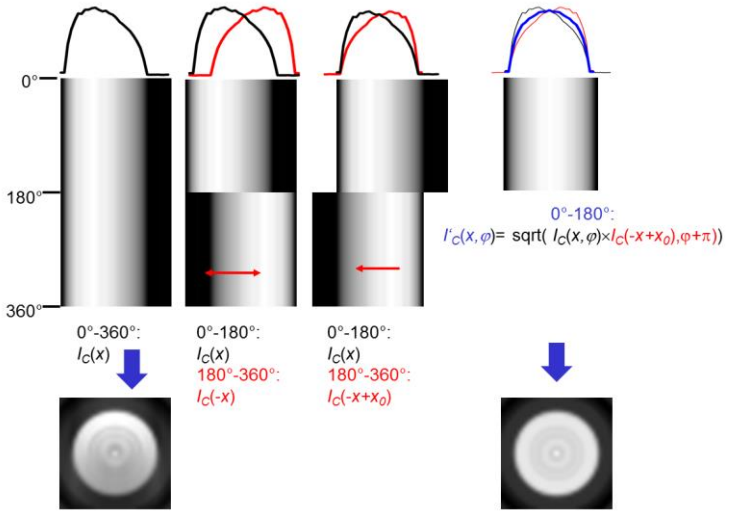

Fig. 6: Correction procedure of asymmetric attenuation of Compton scattering profiles in sinogram of cylinder by averaging profiles at projection angles φ_i and (φ_i +180°) resulting in shorter 180° sinograms of symmetric profiles; resulting reconstructions at bottom.

5. Results – multi materials sample

For further investigation into the properties of Compton tomography by the twin X-ray interaction set-up a cylindrical multi material sample is measured. For current feasibility study a sparse number of 120 projections at 3° angular increments proved to be sufficient. The vertical 9 mm line scans were performed with 10 µm increments. The individual materials arrangement is displayed in Fig. 7, left. The CT reconstruction of the related transmission signals at the attenuation detector is obtained by filtered back projection (Fig. 7, right). Although well defined monochromatic radiation and parallel beam projection nearly free of scattering is achieved, the very weak reconstruction contrast of the PE, wood and PA components demonstrates the weaknesses of conventional attenuation tomography even at moderate differences in materials attenuation.

Fig. 7: Sketch of the multi material sample, a PE tube filled with differently absorbing materials (left) and CT reconstruction of the transmission signals at the attenuation detector obtained by filtered back projection (3° angular increments).

The tomographic intensity sinograms I_A and I_C as obtained from the measurements of the multi material sample and some selected profiles are given by Fig 8. I_A is converted to extinction values µ·d according to Lambert-Beer's law. I_C is treated according to the procedure of Fig. 6. The distorted I_C profiles at 75 and 255° (red and blue lines) compensate for a suitable I'_C profile (green line).

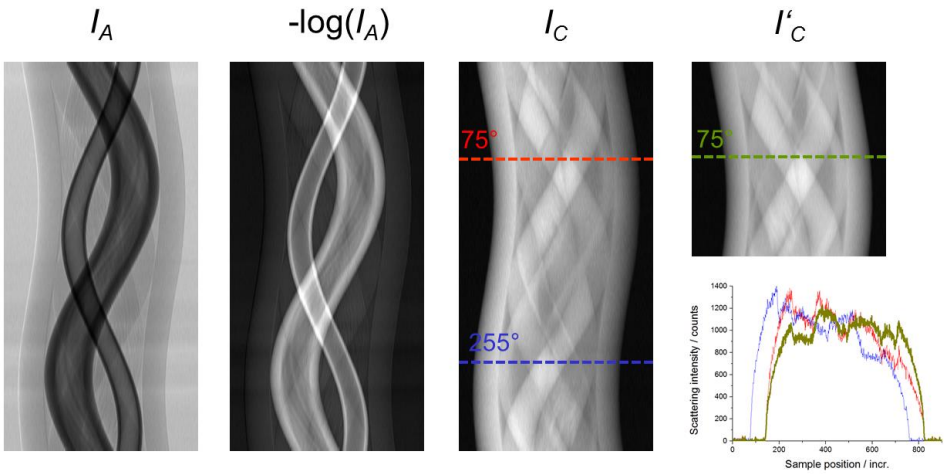

Fig. 8: Intensity sinograms I_A and I_C of 120 projection at 3° intervals as obtained from the measurement (see Fig. 5); I_A converted to µ·d according to Lambert-Beer's law; selected Compton Scattering profiles of I_C treated according to the symmetry procedure of Fig. 6; distorted I_C profiles at 75 and 255° (red and blue lines) compensate to a suitable I_C' profile (green line).

For understanding the very different attenuation and scattering profiles of the sinograms a comparison of X-ray attenuation quantities for carbon, silicon and chlorine is made by Fig. 9. While the incoherent scattering is at roughly the same level for all three elements the

(photoelectric) true absorption differs tremendously. The coherent scattering is of minor interest in the present study. The vertical lines indicate the energy where the incoherent (Compton) scattering cross-section exceeds the absorption cross-section.

Extending the scope of material interactions with matter, neutron attenuation parameters are interesting for comparison, as neutron tomography is well known for its capability of contrasting almost all materials of different atomic numbers simultaneously within in a single reconstruction set. The different interactions of neutrons and X-rays with matter are sketched by Fig. 10 referring to absorption and scattering at electrons and nuclei. At right the very different attenuation parameters of both types of radiation versus atomic numbers are given.

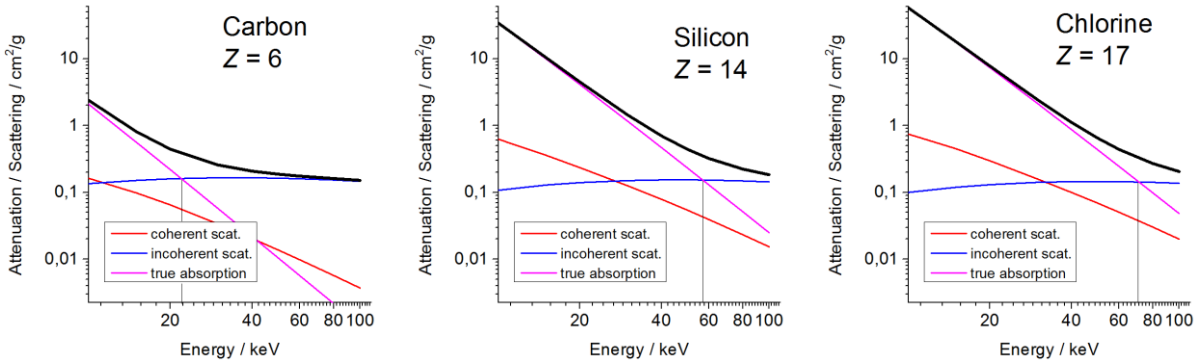

Fig. 9: Comparison of X-ray attenuation quantities for carbon, silicon and chlorine [31]; the incoherent scattering is at roughly the same level for all three elements the (photoelectric) true absorption differs tremendously. The coherent scattering is of minor interest in the present study. The vertical lines indicate the energy where the incoherent (Compton) scattering cross-section exceeds the absorption cross-section.

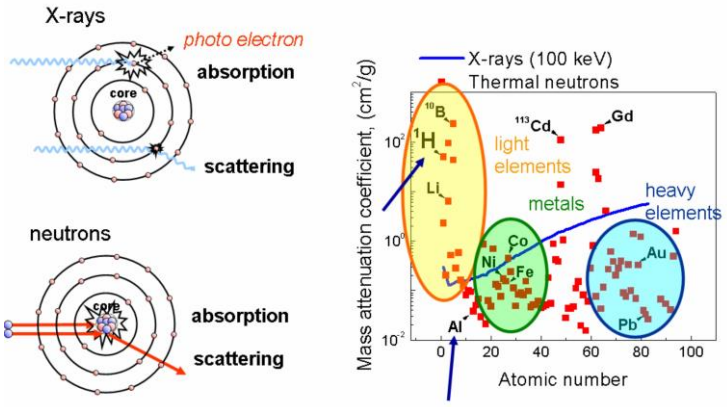

Fig. 10: Different interactions of neutrons and X-rays with matter; left: absorption and scattering at electrons and nuclei; right: very different attenuation of both types of radiation vs. atomic number.

Furthermore, a comparison of neutron and X-ray attenuation quantities for the elements contained in the test sample is made by Table 1.

Neutron tomography was performed at the Helmholtz-Zentrum Berlin für Materialien und Energie (Berlin, Germany) at the cold neutron imaging instrument CONRAD-2 [38]. It provides neutrons with wavelengths between 0.1 nm and 1.2 nm with a maximum at 0.25 nm. The detector system was based on a CCD camera with pixel size 30 µm. The number of the radiographic projections was 300 over 360°.

Tab. 1: Comparison of neutron and X-ray attenuation quantities for the elements contained in the test sample. (neutron data from [37] (1 barn = 10^{-28} m^2), X-ray data from [31]).

Element	Atomic number	**Neutrons**				**17.5 keV X-rays**	
		Scattering length b / 10^{-14} m	Incoherent scattering cross-section σ_{inc} / barn	Absorption cross-section (for λ= 1.8 Å) σ_{abs} / barn		Photo-absorption cross-section τ / cm^2/g	Inelastic cross- section σ_{inc} / cm^2/g
Hydrogen	1	-0.37	79.7	0.33		$4 \cdot 10^{-4}$	0.363
Carbon	6	0.66	< 0.018	0.0033		0.32	0.155
Nitrogen	7	0.94	0.46	1.88		0.55	0.153
Oxygen	8	0.58	< 0.015	< 0.0002		0.91	0.150
Silicon	14	0.41	< 0.017	0.16		6.0	0.135
Chlorine	17	0.96	5.9	33.6		10.8	0.125

The corrected Compton scattering sinogram (intensity I'_C in Fig. 8) is reconstructed by filtered back projection. For a final comparison of the properties of neutron and Compton tomography the reconstruction results obtained from neutron (left) and X-ray Compton (right) tomography are presented by Fig 11. Note that the glass tube is not visible in the neutron result.

Fig. 11: Reconstruction results obtained from neutron (left) and X-ray Compton (right) tomography. Note that the glass tube is not visible in the neutron result.

6. Conclusion

Beyond former approaches of non-destructive Compton scattering inspection by direct localization of the interaction volume based on triangulation [1, 2] we have shown the feasibility of laboratory based Compton CT by twin interaction instrumentation applying 90° Compton scattering and conventional attenuation, simultaneously. In a first approach to reconstruct Compton scattering data by simple correction procedures very different components in a non-metallic composition of materials (atomic numbers up to 17) are highly contrasted at a similar level, which is a well-known (and also shown here) problem for classical attenuation.

Comparison to neutron data reveals similar contrast of the same sample, except for the glass tube, which is solely visible in Compton CT. Future developments regarding Compton CT could be successful in satisfying the increasing demands for imaging compositions of highly different materials. Furthermore, it is considered a promising approach to avoid refractive intensity distortions in high resolution measurements and could replace sophisticated neutron tomography in future.

References

1. V. Romanov, V. Grubsky, N. Patton, T. Jannson: Apodized aperture imaging optics for Compton-scattered x-ray and gamma-ray imaging systems, Proc. SPIE **8144** (2011) 81440M (doi: 10.1117/12.894107).
2. W. Niemann, S. Zahorodny: Status and Future Aspects of X-Ray Backscatter Imaging, Rev. Prog. QNDE. **17A** (1998) 379-385.
3. M.P. Hentschel, R. Hosemann, A. Lange, B. Uther, R. Brückner: Röntgenkleinwinkelbrechung an Metalldrähten, Glasfäden und hartelastischem Polypropylen, Acta Cryst. **A 43** (1987) 506-513.
4. M.P. Hentschel, K.-W.Harbich, A. Lange: Non-destructive evaluation of single-fiber debonding in composites by x-ray refraction, NDT & E Int. **27** (1994) 275-280.
5. K.-W. Harbich, M.P. Hentschel, J. Schors: X-ray refraction characterization of non-metallic materials, NDT&E Int. **34** (2001) 297-302.
6. D. Chapman, W. Thomlinson, R. E. Johnston, D. Washburn, E. Pisano, N. Gmür, Z. Zhong, R. Menk, F. Arfelli, and D. Sayers: Diffraction enhanced x-ray imaging, Phys. Med. Biol. **42** (1997) 2015.
7. S.W. Wilkins, T.E. Gureyev, D. Gao, A. Pogany, A.W. Stevenson: Phase-contrast imaging using polychromatic hard X-rays, Nature **384** (1996) 335–338.
8. V.N. Ingal, E.A. Beliaevskaya: X-ray plane-wave topography observation of the phase contrast from a non-crystalline object, J. Phys. **D 28** (1995) 2314-2317.
9. M. Ando, A. Maksimenko, H. Sugiyama, W. Pattanasiriwisawa, K. Hyodo, C. Uyama: A Simple X Ray Dark- and Bright-Field Imaging Using Achromatic Laue Optics, Jpn. J. Appl. Phys., Part 1, **41** (2002) L1016-L1018.
10. A. Momose: Phase-sensitive imaging and phase tomography using X-ray interferometers, Opt. Express **11** (2003) 2303–2314.
11. F. Pfeiffer, T. Weitkamp, O. Bunk, C. David: Phase retrieval and differential phase-contrast imaging with low-brilliance X-ray sources, Nat. Phys. **2** (2006)258-261.
12. W. Ludwig, P. Cloetens, J. Härtwig, J. Baruchel, B. Hamelin and P. Bastie, Three-dimensional imaging of crystal defects by 'topo-tomography', J. Appl. Cryst. **34** (2001) 602-607
13. A. King, G. Johnson, D. Engelberg, W. Ludwig, J. Marrow: Observations of Intergranular Stress Corrosion Cracking in a Grain-Mapped Polycrystal, Science **312** (2008) 382-385.
14. W. Ludwig, A. King, P. Reischig, M. Herbig, E.M. Lauridsen, S. Schmidt, H. Proudhon S. Forest, P. Cloetens, S. Rolland du Roscoat, J.Y. Buffière, T.J. Marrow, H.F. Poulsen: New opportunities for 3D materials science of polycrystalline materials at the micrometre lengthscale by combined use of X-ray diffraction and X-ray imaging, Mat. Sci. Eng. **A 524** (2009) 69–76.
15. C.G. Schroer: Reconstructing x-ray fluorescence microtomograms, Appl. Phys. Lett. **79** (2001) 1912-1914.
16. A. Simionovici, M. Chukalina, F. Günzler, Ch. Schroer, A. Snigirev, I. Snigireva, J. Tümmler, T. Weitkamp: X-ray microtome by fluorescence tomography, Nucl. Instrum. Meth. **A 467–468** (2001) 889–892.
17. A. Kupsch, A. Lange, M.P. Hentschel, Y. Onel, T. Wolk, A. Staude, K. Ehrig, B.R. Müller, G. Bruno: Evaluating Porosity in Cordierite Diesel Particulate Filter Materials, Part 1 X-Ray Refraction, J. Ceram. Sci. Tech. **4** (2013) 169-176.
18. N. Sunaguchi, T. Yuasa, Q. Huo, S. Ichihara, M. Ando: X-ray refraction-contrast computed tomography images using dark-field imaging optics, Appl. Phys. Lett. **97** (2010) 153701.

19. F.A. Dilmanian, Z. Zhong, B. Ren, X.Y. Wu, L.D. Chapman, I. Orion, W.C. Thomlinson: Computed tomography of x-ray index of refraction using the diffraction enhanced imaging method, Phys. Med. Biol. **45** (2000) 933–946.
20. B.R. Müller, A. Lange, M. Harwardt, M.P. Hentschel, B. Illerhaus, J. Goebbels, J. Bamberg, F. Heutling: Refraction computed tomography, Mater. Test. **46** (2004) 314-319.
21. P. Duvauchelle, G. Peix, D. Babot: Rayleigh to Compton ratio computed tomography using synchrotron radiation, NDT&E Int. **33** (2000) 23–31.
22. R. Cesareo,F. Balogun,A. Brunetti,C. Cappio Borlino: 90° Compton and Rayleigh measurements and imaging, Radiat. Phys. Chem. **61** (2001) 339–342.
23. A. Brunetti, B. Golosio, R. Cesareo: A correction procedure for the self-absorption artifacts in x-ray Compton tomography, X-Ray Spectrom. **31** (2002) 377–382.
24. B.L. Evans, J.B. Martin, L.W. Burggraf, M.C. Roggemann,T.N. Hangartner: Demonstration of energy-coded Compton scatter tomography with fan beams for one-sided inspection, Nucl. Instrum. Meth. **A 480** (2002) 797–806.
25. R. Cesareo, C.C. Borlino, A. Brunetti, B. Golosio, A. Castellano: A simple scanner for Compton tomography, Nucl. Instrum. Meth. **A 487** (2002) 188–192.
26. A. Brunetti, R. Cesareo, B. Golosio, P. Luciano, A. Ruggero: Cork quality estimation by using Compton tomography, Nucl. Instrum. Meth. **B 196** (2002) 161–168.
27. B. Golosio, A. Simionovici, A. Somogyi, L. Lemelle, M. Chukalina, A. Brunetti: Internal elemental microanalysis combining x-ray fluorescence, Compton and transmission tomography, J. Appl. Phys. **94** (2003) 145-156.
28. B. Golosio, A. Brunetti, R. Cesareo: Algorithmic techniques for quantitative Compton tomography, Nucl. Instrum. Meth. **B 213** (2004) 108–111.
29. R. Cesareo, A. Brunetti, B. Golosio, R.T. Lopes, R.C. Barroso, A. Castellano, S. Quarta: Material analysis with a multiple X-ray tomography scanner using transmitted and scattered radiation, Nucl. Instrum. Meth. **A 525** (2004) 336–341.
30. A.H. Compton: Secondary Radiations produced by X-rays and some of their applications to physical problems, Bulletin of the National Research Council. **20** (1922) 10, and A.H. Compton: A quantum theory of the scattering of x-rays by light elements, Phys. Rev. **21** (1923) 483-502.
31. http://physics.nist.gov/PhysRefData/Xcom/
32. http://www.physics.hku.hk/
33. http://www.kutl.kyushu-u.ac.jp/
34. O. Klein, Y. Nishina: Über die Streuung von Strahlung durch freie Elektronen nach der neuen relativistischen Quantendynamik von Dirac, Z. Phys. **52** (1929) 853-868.
35. M. Zhukovsky, S. Podoliako, G.-R. Tillack, C. Bellon: Monte Carlo simulation of photon transport coupled to cad object description, Rev. Prog. QNDE. **23** (2004) 515-521.
36. J.H. Hubbell, W.J. Veigele, E.A. Briggs, R.T. Brown, D.T. Cromer, R.J. Howerton,: Atomic Form Factors, Incoherent Scattering Functions, and Photon Scattering Cross Sections. J. Phys. Chem. Ref. Data **4** (1975) 471-538; erratum in **6** (1977) 615-616.
37. K. Hardman-Rhyne, N.F. Berk, E.R. Fuller, Jr.: Microstructural Characterization of Ceramic Materials by Small Angle Neutron Scattering Techniques, J. Res. Nat. Bur. Stand. **89** (1984) 17-34.
38. N. Kardjilov, A. Hilger, I. Manke, M. Strobl, M. Dawson, S. Williams, J. Banhart: Neutron tomography instrument CONRAD at HZB, Nucl. Instrum. Meth. **A 651** (2011) 47-52.